Int J Adv Manuf Technol (2014) 71:1159–1174
DOI 10.1007/s00170-013-5554-0

ORIGINAL ARTICLE

# Chatter stability for micromilling processes with flat end mill

**Qinghua Song · Zhanqiang Liu · Zhenyu Shi**

Received: 1 August 2013 / Accepted: 9 December 2013 / Published online: 3 January 2014
© Springer-Verlag London 2014

**Abstract** A mechanistic model is developed to predict micromilling forces with flat end mill for both shearing and ploughing-dominant cutting regimes. The model assumes that there is a critical chip thickness that determines whether a chip will form or not. Numerical method is extended to predict the chatter stability in micro end milling, which is performed based on the proposed cutting force model. The simulating procedure for predicting stability and cutting forces is presented in detail, and the stability diagram is constructed. The validation experiments are conducted to verify the simulation results. Both experimental cutting forces measured and machined workpiece surface scanned through digital microscope are analyzed and used to verify the proposed model.

**Keywords** Micromilling · Cutting force · Chatter · Stability

**Nomenclature**

| | |
|---|---|
| $m_x$, $m_y$ | Masses in $x$ and $y$ directions |
| $c_x$, $c_y$ | Damping in $x$ and $y$ directions |
| $k_x$, $k_y$ | Stiffness in $x$ and $y$ directions |
| $q_x(t)$, $q_y(t)$ | Displacements in $x$ and $y$ directions |
| $F_x(t)$, $F_y(t)$, and $F_z(t)$ | Cutting forces over all of the teeth in $x$, $y$, and $z$ directions |
| $\eta$ | Helix angle of the flank edge |
| $\Delta F^j_{\mathrm{c}}(t), \Delta F^j_{\mathrm{n}}(t), \Delta F^j_{\mu}(t)$ | Cutting forces components for cutting tooth $j$ at location $z$ on the tool, in the refined orthogonal cutting method for shear-dominant regime |
| $\Delta F^j_{\mathrm{rc}}(t), \Delta F^j_{\mathrm{tc}}(t), \Delta F^j_{\mathrm{zc}}(t)$ | Radial, tangential, and axial edge force components for cutting tooth $j$ at location $z$ on the tool for shear-dominant regime |
| $\Delta F^j_{\mathrm{re}}(t), \Delta F^j_{\mathrm{te}}(t), \Delta F^j_{\mathrm{ze}}(t)$ | Radial, tangential, and axial edge force components for cutting tooth $j$ at location $z$ on the tool for both shear-dominant and ploughing-dominant regimes |
| $\Delta F^j_{\mathrm{rp}}(t), \Delta F^j_{\mathrm{tp}}(t), \Delta F^j_{\mathrm{zp}}(t)$ | Radial, tangential, and axial ploughing force components for cutting tooth $j$ at location $z$ on the tool for ploughing-dominant regime |
| $\Delta F^j_x(z,t), \Delta F^j_y(z,t), \Delta F^j_z(z,t)$ | Cutting force components for cutting tooth $j$ at location $z$ in $x$, $y$, and $z$ directions |
| $F^j_x(t), F^j_y(t), F^j_z(t)$ | Cutting force components for cutting tooth $j$ in $x$, $y$, and $z$ directions |
| $\Delta z$ | Thickness of each infinitesimal disk element in the axial direction |
| $K_{\mathrm{tc}}$ | Specific cutting energy |
| $k_{\mathrm{nc}}$ | Proportionality constant |
| $\mu_{\mathrm{c}}$ | Friction coefficient for the sliding motion between the inner surface of chip and the front rake face of the tooth |
| $C_{\mathrm{p}}$ | Viscous damping coefficient that is associated with process damping |

Q. Song (✉) · Z. Liu · Z. Shi
Key Laboratory of High Efficiency and Clean Mechanical Manufacture, Ministry of Education, School of Mechanical Engineering, Shandong University, Jinan, People's Republic of China
e-mail: ssinghua@sdu.edu.cn

Z. Liu
e-mail: melius@sdu.edu.cn

| | |
|---|---|
| $\gamma_n$ | Normal rake angle of the cutting tooth |
| $h(t, j, z)$ | Dynamic uncut chip thickness for the *j*th flute of the cutter at time *t* and height *z* |
| $\varphi(t, j, z)$ | Angular position of tooth *j* at axial location *z* and time *t* |
| $\varphi_0$ | Initial angular position of the first tooth at $z=0$ |
| $\dot{h}(t, j, z)$ | Time rate of change of the dynamic uncut chip thickness |
| $\tau 1$, $\tau 2$ | Time delays in *x* and *y* directions |
| $N$ | Number of tooth |
| $R$ | Radius of tool |
| $F$ | Feed rate per tooth |
| $\Omega$ | Rotating angular velocity |
| $K_{re}$, $K_{te}$, $K_{ae}$ | Radial, tangential, and axial edge coefficients |
| $K_{rpc}$, $K_{tpc}$, $K_{apc}$ | Radial, tangential, and axial ploughing coefficients |
| $\Delta V_p$ | Ploughing volume for a discretized disk element of a micro end mill flute |
| $A_p$ | Interference area |
| $r_e$ | Edge radius |
| $h_{er}$ | Elastic recovery |
| $h_c$ | Minimum chip thickness |
| $\beta_e$ | Clearance angle |
| $r_o$ | Runout |

## 1 Introduction

Highly accurate miniaturized components that are made up of a variety of engineering materials drastically increased micro end milling operation applications in the conventional shop floor [1]. The flexibility and efficiency of micromachining processes using miniature cutting tools allows for the economical fabrication of smaller batch sizes compared with other processes [2]. Currently, tools with a diameter of 1 mm or below are regarded as micro tools and recently micro tools with a diameter of 0.05 mm or less began to be produced commercially [3]. As with macromachining operations, micromachining processes also exhibit an unstable phenomenon called regenerative chatter [4, 5], due to changes in the chip thickness. Chatter can cause serious damage in the micro scale, since the tolerances are generally tight and small vibrations can break the tool and ruin the part.

Micromachining phenomena differs from macro machining due to size effects, which occur because the edge radius of micro tools is comparable to the uncut chip thickness, resulting in large negative rake angles [6]; as a result, the so-called minimum chip thickness phenomenon occurs in micromachining. Thus, when the uncut chip thickness is less than the minimum chip thickness, no chip formation occurs and only ploughing/rubbing takes place. Material separation occurs when the uncut chip thickness is greater than the critical minimum chip thickness, or at what is sometimes referred to as the stagnation point [7], when the material above the minimum chip thickness forms a chip and the material below the minimum chip thickness deforms under the edge with a partial elastic recovery, resulting in material ploughing.

Many researchers have investigated the size effect, minimum chip thickness, and edge radius size, and so on. Lai et al. [8] proposed a modeling method of micro scale milling considering size effect, micro cutter edge radius and minimum chip thickness. Bissacco et al. [9] predicted the cutting force of micromilling including the cutting edge radius size. Shi et al. [10] simulated the minimum uncut chip thickness for micromachining with different rake angle. Liu et al. [11] investigated the material strengthening mechanisms and their contribution to size effect in microcutting.

In order to understand the micromilling mechanisms, cutting force models have been developed by many researchers. Vogler et al. [12] made the first attempt at incorporating the effect of minimum chip thickness into a micro end milling force model by using the slip-line plasticity model. Jun et al. [13] developed a more complicated slip-line plasticity model that accounts for elastic–plastic deformation and elastic recovery. Fang et al. [14] also developed a universal slip-line model for rounded-edge tools. The finite element model approach has also been utilized by many researchers to model the microcutting process and to understand size effect [11], machining stresses [7], and the influence of cutting edge radius on minimum uncut chip thickness [10]. However, the majority of these methods require many assumptions, and the parameters used in the model are difficult to estimate. There are a few mechanistic models developed for micro end milling processes [15–17], but these models do not consider the effects of edge radius, minimum chip thickness, and elastic recovery together.

Many researchers have also investigated the chatter stability of micromilling process. Lakshmi et al. [18] developed an algorithm to construct the stability lobe diagram for both high-speed milling and micromilling. While the algorithm has the lower precision for prediction of micromilling stability because the cutting force model used does not include the size effect. Shi et al. [19] investigates the gyroscopic and mode interaction effects on the micro end mill dynamics and the stability behavior due to regenerative chatter. Afazov et al. [20]

presented a new approach for chatter modeling in micromilling, which takes into account: the nonlinearity of the uncut chip thickness including the runout effect; velocity dependent micromilling cutting forces; the dynamics of the toolholder-spindle assembly. The researches above almost extended directly the macro analysis method to the micro field. Many influence factors in micromilling operation are not considered, such as size effect. As presented above, when the chip actually forms during cutting with a finite edge radius tool, ploughing under the edge contributes to an increase in the specific energy. Additionally, the edge radius of micro tools is comparable to the uncut chip thickness, resulting in large negative rake angles [6]. This is particularly evident at low feed rates, where the effects of ploughing are more significant [21], also known as damping effects.

Process damping can increase stability, especially at low spindle speeds, which occurs because elastic recovery increases the friction between the flank face of the tool and the workpiece and amplifies the effect of process damping. Shi et al. [22] investigated the influences of damping properties, clamping conditions, and the shank length of micro end mills by experiments and analytical solutions. This paper presents a new measuring method for online chatter detection using external excitations via piezoelectric actuators. Tajalli et al. [23] investigated the chatter instability of micro end mill tools by taking into account the process damping effect. Timoshenko beam theory and the extended Hamilton's Principle were used to formulate a detailed dynamical model of the rotating micro end mill. An exact dynamic stiffness method was developed to investigate modal characteristics of the tool including mode shapes to be utilized as base functions for the solution. Rahnama et al. [24] investigated the chatter suppression in micro end milling with process damping, which occurs because the friction between the tool and workpiece, especially at low spindle speeds. Park et al. [25] employed the robust chatter stability theorem, which is based on the edge theorem, to provide the robust stability within the minimum and maximum boundaries of changing parameters in micromilling operations. In their model, the process damping force was assumed to be proportional to the volume of the deformed workpiece material under the clearance face of the tool.

Additionally, in micro end milling, the ratio of feed per tooth to tool radius is considerably higher compared with conventional end milling. When machining is performed at high feed rates, the effects of ploughing and elastic recovery are insignificant enough to ignore, and the cutting mechanism is considered to be shearing [21]. While in milling operations, the feed motion will affect the cutting duration and results in a trochoidal tool path. The entry angle for up-milling will be advanced and the exit angle for down-milling will be delayed due to feed [26]. And the time delays in feed direction and perpendicular to the feed direction are different due to the feed motion [27]. Therefore, the cutting force model for the shearing-dominant regime should consider the effect of feed rate on both the entry/exit angles of flute and time delays in two directions.

The objectives of this paper are developing a mechanistic model to predict micromilling forces for both shearing and ploughing-dominant cutting regimes, and presenting the simulating procedure for predicting stability and cutting forces. Thus, the organization of the paper is as follows: Section 2 depicts the dynamic model of micromilling process. Section 3 describes the experimental setup. Section 4 illustrates the methodology for predicting stability of micromilling process including shearing and ploughing-dominant cutting forces, and milling tests are conducted to validate the numerical simulation results. Section 5 concludes with the contributions.

## 2 Dynamic model of micromilling process

The tool is assumed to be flexible relative to the rigid workpiece. Micromilling tool with radius $R$ (millimeter) and the number $N$ of teeth can be considered to have two orthogonal degrees of freedom as shown in Fig. 1, $a_e$ is the radial depth of cut, and $\Omega$ is the constant rotational angular velocity. If the tool is modeled as a symmetric beam, its modal matrices are diagonal with the same diagonal values. In practice, however, the tool is not perfectly symmetric due to the helical flutes, and the modal matrices are not diagonal. In this case, an accurate modeling results in time periodic modal matrices due to the rotation of the flexible tool. However, the tool can

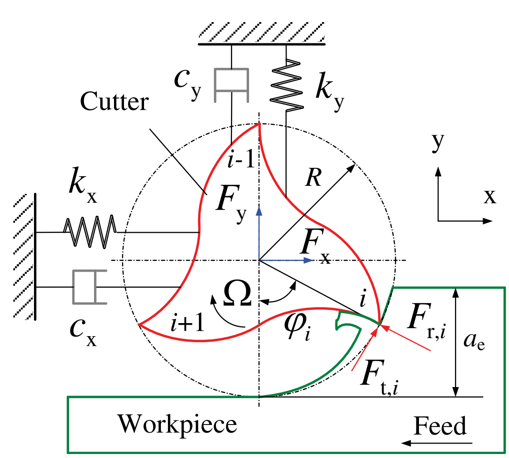

**Fig. 1** 2-DOF micromilling model

usually be considered almost symmetric and the cross terms in the modal matrices can be neglected. The governing equation for the 2-DOF oscillator of micromilling process has the form

$$\begin{bmatrix} m_x & 0 \\ 0 & m_y \end{bmatrix}\begin{Bmatrix} \ddot{q}_x \\ \ddot{q}_y \end{Bmatrix} + \begin{bmatrix} c_x & 0 \\ 0 & c_y \end{bmatrix}\begin{Bmatrix} \dot{q}_x \\ \dot{q}_y \end{Bmatrix} + \begin{bmatrix} k_x & 0 \\ 0 & k_y \end{bmatrix}\begin{Bmatrix} q_x \\ q_y \end{Bmatrix} = \begin{Bmatrix} F_x \\ F_y \end{Bmatrix} \quad (1)$$

where, $m_x$, $m_y$, $c_x$, $c_y$, $k_x$, $k_y$, $q_x$, $q_y$, $F_x$, and $F_y$ are the mass, damping, stiffness, displacements and cutting forces in $x$ and $y$ directions, respectively.

A mechanistic model is developed to predict micromilling forces for both shearing and ploughing-dominant cutting regimes. The model assumes that there is a critical chip thickness that determines whether a chip will form or not. On the one hand, when machining is performed at high feed rates, the effects of ploughing and elastic recovery are insignificant enough to ignore, and the cutting mechanism is considered to be shearing [21]. While in milling operations, the feed motion will affect the cutting duration and results in a trochoidal tool path. The entry angle for up-milling will be advanced and the exit angle for down-milling will be delayed due to feed. And the time delays in feed direction and perpendicular to the feed direction are different due to the feed motion. On the other hand, at lower feed rates, the effects of ploughing and elastic recovery are substantial and need to be taken into account.

## 2.1 Cutting force model for the shearing-dominant regime

When the chip thickness is larger than the critical value, the cutting mechanism is assumed to be similar to the conventional cutting mechanism that considers the shearing and edge coefficients.

Here, process damping, which can be modeled as resulting in a viscous damping force that is proportional to the time derivative of the uncut chip thickness in a manner similar to Ref. [27], is also considered in the cutting force formulation.

The cutter is modeled as the sum of a stack of infinitesimal disk elements each with a thickness $\Delta z$ [28]. The cutting force components associated with this disk element, at time $t$, for cutting tooth $j$, and at axial location $z$ on the tool, are represented by $\Delta F_r^j$ for the radial direction, $\Delta F_t^j$ for the tangential direction, and $\Delta F_z^j$ for the axial direction, which can be modeled as follows, when the uncut chip thickness is greater than the minimum chip thickness value:

$$\begin{Bmatrix} \Delta F_r^j(t) \\ \Delta F_t^j(t) \\ \Delta F_z^j(t) \end{Bmatrix} = \begin{bmatrix} 1 & 0 & 0 \\ 0 & \cos\eta & \sin\eta \\ 0 & -\sin\eta & \cos\eta \end{bmatrix}\begin{Bmatrix} \Delta F_n^j(t) \\ \Delta F_c^j(t) \\ \Delta F_\mu^j(t) \end{Bmatrix} \quad (2)$$

where, $\eta$ is the helix angle. $\Delta F_c^j$, $\Delta F_n^j$, and $\Delta F_\mu^j$ are the cutting forces components in the refined orthogonal cutting method [27], which can be expressed as

$$\begin{Bmatrix} \Delta F_n^j(t) \\ \Delta F_c^j(t) \\ \Delta F_\mu^j(t) \end{Bmatrix} = \begin{bmatrix} k_{nc}K_{tc} & k_{nc}C_p \\ K_{tc} & C_p \\ \mu_c K_{tc}\cos\gamma_n - \mu_c k_{nc} K_{tc}\sin\gamma_n & \mu_c C_p\cos\gamma_n - \mu_c k_{nc} C_p \sin\gamma_n \end{bmatrix}\begin{Bmatrix} h(t,j,z) \\ \dot{h}(t,j,z) \end{Bmatrix}\frac{\Delta z}{\cos\eta} \quad (3)$$

where $K_{tc}$ is the specific cutting energy and $k_{nc}$ is a proportionality constant. $\mu_c$ is the friction coefficient for the sliding motion between the inner surface of chip and the front rake face of the tooth. $C_p$ is the viscous damping coefficient that is associated with process damping. They are related to the cutting geometry, the material properties, and the cutting conditions. $\gamma_n$ is the normal rake angle of the cutting tooth. $h(t, j, z)$ is the dynamic uncut chip thickness for the $j$th flute of the cutter at time $t$ and height $z$,

$$h(t,j,z) = [q_x(t) - q_x(t-\tau_1) + \tau_1 f]\sin\varphi(t,j,z) + \left[q_y(t) - q_y(t-\tau_2)\right]\cos\varphi(t,j,z) \quad (4)$$

Here, the variable $\varphi(t, j, z)$, which is the angular position of tooth $j$ at axial location $z$ and time $t$, is determined by

$$\varphi(t,j,z) = \Omega t - (i-1)\frac{2\pi}{N} - \frac{\tan\eta}{R}z + \varphi_0 \quad (5)$$

where, $\varphi_0$ is the initial angular position of the first tooth at $z$=0.

$\dot{h}(t,j,z)$ is the time rate of change of the dynamic uncut chip thickness, which can be obtained by deriving Eq. (4).

$$\dot{h}(t,j,z) = \left[\dot{q}_x(t) - \dot{q}_x(t-\tau_1) - \left(q_y(t) - q_y(t-\tau_2)\right)\Omega\right]\sin\theta(t,j,z) + \left[(q_x(t) - q_x(t-\tau_1) + \tau_1 f)\Omega + \dot{q}_y(t) - \dot{q}_y(t-\tau_2)\right]\cos\theta(t,j,z) \quad (6)$$

The time delays $\tau_1$ and $\tau_2$ in $x$ and $y$ direction are different because of the feed, which can be expressed as [27]

$$\tau_1 = \frac{2\pi}{N\Omega}, \tau_2 = \frac{4\pi R}{N(2\Omega R + f)} \tag{7}$$

where, $N$ is the number of tooth. $R$ is the radius of tool. $f$ is the feed rate per tooth. $\Omega$ is the rotating angular velocity.

Additionally, edge forces are assumed to proportional with edge length, can be expressed as

$$\begin{Bmatrix} \Delta F^j_{\mathrm{re}}(t) \\ \Delta F^j_{\mathrm{te}}(t) \\ \Delta F^j_{\mathrm{ze}}(t) \end{Bmatrix} = \begin{Bmatrix} K_{\mathrm{re}} \\ K_{\mathrm{te}} \\ K_{\mathrm{ae}} \end{Bmatrix} \Delta z \tag{8}$$

For the infinitesimal disk element, the cutting forces including the edge forces are obtained as

$$\begin{Bmatrix} \Delta F^j_{\mathrm{r}}(t) \\ \Delta F^j_{\mathrm{t}}(t) \\ \Delta F^j_{\mathrm{z}}(t) \end{Bmatrix} = \left( \begin{bmatrix} k_1 K_{\mathrm{tc}} & k_1 C_{\mathrm{p}} \\ k_2 K_{\mathrm{tc}} & k_2 C_{\mathrm{p}} \\ k_3 K_{\mathrm{tc}} & k_3 C_{\mathrm{p}} \end{bmatrix} \begin{Bmatrix} h(t,j,z) \\ \dot{h}(t,j,z) \end{Bmatrix} + \begin{Bmatrix} K_{\mathrm{re}} \\ K_{\mathrm{te}} \\ K_{\mathrm{ae}} \end{Bmatrix} \right) \Delta z \tag{9}$$

here

$$k_1 = \frac{k_{\mathrm{nc}}}{\cos\eta}, k_2 = 1 + \mu_{\mathrm{c}} \tan\eta\,(\cos\gamma_{\mathrm{n}} - k_{\mathrm{nc}} \sin\gamma_{\mathrm{n}}), k_3 = -\tan\eta + \mu_{\mathrm{c}}(\cos\gamma_{\mathrm{n}} - k_{\mathrm{nc}} \sin\gamma_{\mathrm{n}}) \tag{10}$$

where $K_{\mathrm{re}}$, $K_{\mathrm{te}}$, and $K_{\mathrm{ae}}$ are the radial, tangential, and axial edge coefficients, respectively.

### 2.2 Cutting force model for the ploughing-dominant regime

Chip formation does not occur when the uncut chip thickness is less than the minimum chip thickness; instead, there is ploughing and partial elastic recovery of the material. In the ploughing-dominant regime, the micromill undergoes both ploughing and shearing during the removal process. The cutting force in the ploughing-dominant regime is modeled based on the model introduced by Malekian et al. for the forces in micromilling operation [21]. The ploughing forces are modeled as proportional to the volume of interference between the tool and the workpiece, considering the effect of the elastic recovery.

For a discretized disk element of a micro end mill flute, the ploughing volume can be expressed as $V_{\mathrm{p}}=A_{\mathrm{p}}\Delta z$. Since the ploughing forces can be modeled as proportional to the volume of interference between the tool and the workpiece, the radial, tangential and axial ploughing forces can be written as a multiplication of a constant and the ploughed volume. Therefore, the ploughing forces for each differential flute element can be computed as

$$\begin{Bmatrix} \Delta F^j_{\mathrm{rp}}(t) \\ \Delta F^j_{\mathrm{tp}}(t) \\ \Delta F^j_{\mathrm{zp}}(t) \end{Bmatrix} = \left( \begin{Bmatrix} K_{\mathrm{rpc}} \\ K_{\mathrm{tpc}} \\ K_{\mathrm{apc}} \end{Bmatrix} A_{\mathrm{p}} + \begin{Bmatrix} K_{\mathrm{re}} \\ K_{\mathrm{te}} \\ K_{\mathrm{ae}} \end{Bmatrix} \right) \Delta z \tag{11}$$

where $K_{\mathrm{rpc}}$, $K_{\mathrm{tpc}}$, and $K_{\mathrm{apc}}$ are the radial, tangential, and axial ploughing coefficients, respectively. The interference area $A_{\mathrm{p}}$ is a function of the edge radius $r_{\mathrm{e}}$, the chip thickness $h$, the elastic recovery $h_{\mathrm{er}}$, and the clearance angle $\beta_{\mathrm{e}}$, as depicted in [21]. An elastic recovery rate of 10 % is considered for the aluminum workpiece in this study.

The ploughing cutting forces are formulated based on the interference volume between the tool and workpiece [13]. When the chip thickness becomes larger than the critical chip thickness, chip formation starts. Forces in this region can be described based on the conventional shearing cutting models.

The ploughing coefficients represent ploughing of the workpiece material. $K_{\mathrm{re}}$, $K_{\mathrm{te}}$, and $K_{\mathrm{ae}}$ are the same edge coefficients as in Eq. (8). Since the edge coefficients represent friction as the uncut chip thickness goes to zero, the edge components in the ploughing-dominant regime must be the same as those in the shearing-dominant regime [21].

Therefore, the radial, tangential, and axial forces acting on a discretized disk element for the $j$th flute of the cutter at time $t$ can be expressed as

$$\begin{Bmatrix} \Delta F^j_{\mathrm{r}}(t) \\ \Delta F^j_{\mathrm{t}}(t) \\ \Delta F^j_{\mathrm{z}}(t) \end{Bmatrix} == \begin{cases} \left( \begin{bmatrix} k_1 K_{\mathrm{tc}} & k_1 C_{\mathrm{p}} \\ k_2 K_{\mathrm{tc}} & k_2 C_{\mathrm{p}} \\ k_3 K_{\mathrm{tc}} & k_3 C_{\mathrm{p}} \end{bmatrix} \begin{Bmatrix} h(t,j,z) \\ \dot{h}(t,j,z) \end{Bmatrix} + \begin{Bmatrix} K_{\mathrm{re}} \\ K_{\mathrm{te}} \\ K_{\mathrm{ae}} \end{Bmatrix} \right) \Delta z & h > h_{\mathrm{c}} \\ \left( \begin{Bmatrix} K_{\mathrm{rpc}} \\ K_{\mathrm{tpc}} \\ K_{\mathrm{apc}} \end{Bmatrix} A_{\mathrm{p}} + \begin{Bmatrix} K_{\mathrm{re}} \\ K_{\mathrm{te}} \\ K_{\mathrm{ae}} \end{Bmatrix} \right) \Delta z & 0 < h \le h_{\mathrm{c}} \end{cases} \tag{12}$$

Since the cutting forces in the axial direction are small compared with the planar directions, only the forces in the $x$ and $y$ directions have been considered in this study. The limit $\Delta z \to 0$ is considered, and

**Table 1** The dynamic characteristics at the tool tip

| Mode number | $x$ direction | | | $y$ direction | | |
|---|---|---|---|---|---|---|
| | $\omega_n$ (Hz) | $\zeta$ | $k$ (N/m) | $\omega_n$ (Hz) | $\zeta$ | $k$ (N/m) |
| 1 | 680 | 0.006 | $2.30\times10^6$ | 620 | 0.005 | $6.85\times10^6$ |
| 2 | 1,450 | 0.026 | $4.21\times10^5$ | 1,310 | 0.030 | $3.96\times10^5$ |

transforming the cutting forces from the cutter coordinates to the global coordinates and integrating with respect to $z$ and summing the cutting forces over all of the $N$ number of teeth, resulting in

$$\mathbf{F}(t) = \begin{cases} \mathbf{K}(t)\mathbf{q}(t) - \mathbf{K}(t)\mathbf{q}(t-\tau_{1,2}) + \widehat{\mathbf{K}}(t)\tau_1 f + \mathbf{C}(t)\dot{\mathbf{q}}(t) - \mathbf{C}(t)\dot{\mathbf{q}}(t-\tau_{1,2}) + \mathbf{E}(t) & h > h_c \\ \mathbf{P}(t)A_p + \mathbf{E}(t) & 0 < h \le h_c \end{cases} \tag{13}$$

The derivation of Eq. (13) is shown in Appendix, in detail. Note that, the dynamic equation presented in Appendix is a 4DOF model, in which the flexible of workpiece is also included.

## 3 Experiments analysis

There are three different types of experiments presented in this paper: dynamic tests, cutting tests and chatter tests. All the experiments are performed on the micromilling machines in Key Laboratory of High Efficiency and Clean Mechanical Manufacture at the Shandong University. The machining center used for this study is an ultra precision vertical CNC milling machine (Kern Micro 2522) with a spindle that can rotate up to 50,000 rpm.

1. Dynamic tests The experimental modal analysis (EMA) is performed to obtain the dynamics of the micromilling machines. To obtain the dynamics of spindle and milling machine, a series of conventional impact hammer tests are performed in this research. To excite the structure, a miniature impact hammer (LC-01A) is employed. The deflection is measured using a laser sensor (Keyence LK-G30) with a resolution of 10 nm, minimum sample period of 20 µs. Other sensors, e.g., capacitance or eddy current displacement sensors cannot be used because of the smaller diameter of mill cutter. And the weight of the accelerometer may affect the measurements even though it may be a miniature accelerometer. The data is collected through a LK-Navigator software supported by the Keyence corporation. And the collected data is analyzed by Matlab toolbox, which contains an embedded anti-aliasing filter that prevents

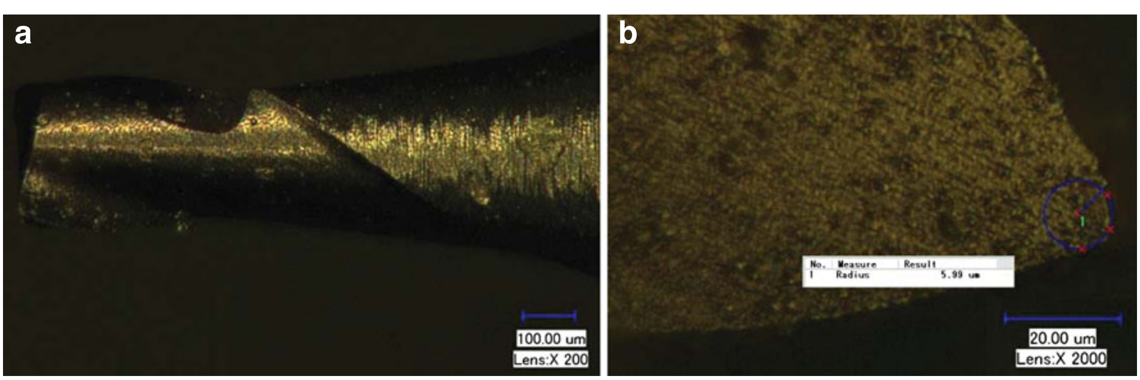


Side view of end mill Tool edge radius

**Fig. 2** Photographs of the miniature end mill the data to be contaminated by the very high frequency noise. The modal parameters are listed in Table 1.

2. Cutting tests The cutting tests are carried on to identify the cutting constants in the micromilling operation including cutting coefficients, edge coefficients, ploughing coefficients. The chatter stability analysis in this research is based on accurate measurement of dynamics and cutting coefficients.

All the cutting and chatter tests were performed on Al 7075, with a tungsten carbide (WC) flat end mills. To have a more precise estimation of the forces and cutting mechanisms, the tool dimensions are investigated through Digital Microscope (Keyence VHX-600ESO) located at the Shandong University. The pictures for the edge and tool radius are presented in Fig. 2 with lens ×200 and ×2,000, respectively. The radial runout influences the effective feed rate experienced by an individual tooth. Upon clamping, the endmill in the toolholder and clamping the toolholder assembly on the spindle, a static measurement of runout can be taken using a dial indicator. The total indicated reading can be used as a measure of the radial runout. The relative runout between successive teeth governs the effective feed experienced by each tooth. The tooth having the highest point would experience the maximum effective feed per tooth. The required dimensional and geometrical characteristics of the tool are presented in Table 2. The edge radius of the tool is 6 μm, and it has been shown that the critical chip thickness for aluminum is approximately 1 μm [29]. The acceleration is simultaneously measured using two acceleration sensors mounted on the spindle in the $x$ and $y$ directions, respectively.

Cutting coefficients are one of the major factors affecting the chatter stability. A set of experiments is performed on Kern Micro 2522 to obtain the cutting, edge and ploughing coefficients in micromilling operation. A miniature table Kistler dynamometer is used to accurately measure the cutting forces. The data were acquired for 200,000 samples/s using a data acquisition system (Dynwave Type 2825D-02). The root mean square (RMS) of the forces was employed. The mechanistic cutting coefficients are shown in Table 3. The frictional coefficient is selected as 0.2 [27], and process damping coefficient is 0.01 [29].

**Table 2** Tool tip geometry

| Tool tip geometries | Tool tip parameters |
|---|---|
| Tool radius (μm), $R$ | 300 |
| Tool edge radius (μm), $r_e$ | 6 |
| Clear angle on flat surface, $\beta_e$ | 10° |
| Runout (μm), $r_o$ | 0.1, 0.15 |

3. Chatter tests To valid the stability results, chatter tests are conducted under selected 15 cutting cases. The radial depth of cut is 0.3 mm (slot milling), the feed per tooth is 0.001 mm, and other cutting parameters for chatter tests are shown in Table 4. Before the chatter tests, the workpiece surface is flatted through the flat end mill with diameter 6 mm. The experimental setup for micromilling tests is shown in Fig. 3.

## 4 Stability analyses and discussions

Substituting Eq. (13) (only considering the forces in the $x$ and $y$ directions) into Eq. (1), 2-DOF dynamic model of micromilling process is obtained, which is a non-smooth differential equation. When $h>h_c$, it is a delay differential equation with two time delays for regenerative chatter vibration, when $0<h\leq h_c$, while, it is an inhomogeneous differential equation for forced vibration, and when $h\leq 0$, the cutting forces are zero, Eq. (1) is an inhomogeneous differential equation for free vibration.

Edge coefficients act as static components for the cutting forces and do not influence stability [4]. Hence, the static forces due to edge coefficients have been neglected in the stability study. The stability of Eq. (1) can be predicted by using numerical methods [4, 30, 31]. The flow chart for predicting the stability is shown in Fig. 4. The simulating procedure for cutting force (red thin arrowed lines) and stability (blue bold arrowed lines) is stated as follows:

Step 1 Determine the initial parameters, control variables, and simulating accuracy, including cutting

**Table 3** Mechanistic cutting coefficients

| $k_{nc}$ | $K_{tc}$ (N/m$^2$) | $K_{te}$ (N/m) | $K_{re}$ (N/m) | $K_{tpc}$ (N/m$^3$) | $K_{rpc}$ (N/m$^3$) |
|---|---|---|---|---|---|
| 0.68 | $3.440\times10^9$ | $1.9\times10^3$ | $1.3\times10^3$ | $7.9\times10^{11}$ | $1.21\times10^{12}$ |

**Table 4** Cutting parameters for chatter tests

| No. of cases | | Axial depth of cut (mm) | | |
|---|---|---|---|---|
| | | 0.01 | 0.03 | 0.05 |
| Spindle speed (rpm) | 10,000 | (a) | (f) | (k) |
| | 15,000 | (b) | (g) | (l) |
| | 20,000 | (c) | (h) | (m) |
| | 25,000 | (d) | (i) | (n) |
| | 30,000 | (e) | (j) | (o) |

conditions ($a_e$, $a_p$, $n$, $f_z$, down- or up-milling), dynamic parameters ($k_x$, $k_y$, $c_x$, $c_y$, $m_x$, $m_y$), cutter geometries ($D$, $N$, $\eta$, $\gamma_n$, $r_e$, $\beta_e$), and cutting constants ($k_{nc}$, $K_{tc}$, $K_{te}$, $K_{ne}$, $K_{tpc}$, $K_{npc}$, $\mu_c$, $C_p$, $h_c$), and so on;

Step 2 For each ($n$, $a_p$), calculate cutting thickness of $j$th with $z$ at different flute location, Eqs. (4) and (5), excluding regenerative displacements;

Step 3 If $h>h_c$, the first cutting force model in Eq. (13) is used to simulating the cutting forces and predicting the stability; if $0<h\leq h_c$, the second cutting force model in Eq. (13) is used to simulating the cutting forces only;

Step 4 Identify the $j$ and $z$, if the $j>N$ or $z>a_p$, break, and calculate the next ($n$, $a_p$).

Step 5 Obtain and show the results for stability analysis or cutting forces.

Note that, when simulating the cutting forces, the control variables $n$ and $a_p$ are both the single value (e.g., $n$=10, 000 rpm; $a_p$=0.1 mm); while, they are both scale values (e.g., $n$=2,000~20,000 rpm; $a_p$=0.001~0.5 mm) for predicting the stability in order to obtain the stability limit diagrams.

The stability diagram constructed based on the above simulating procedure is shown in Fig. 5. The cases listed in Table 4 are all labeled in Fig. 5. It can be seen that, the cases labeled in

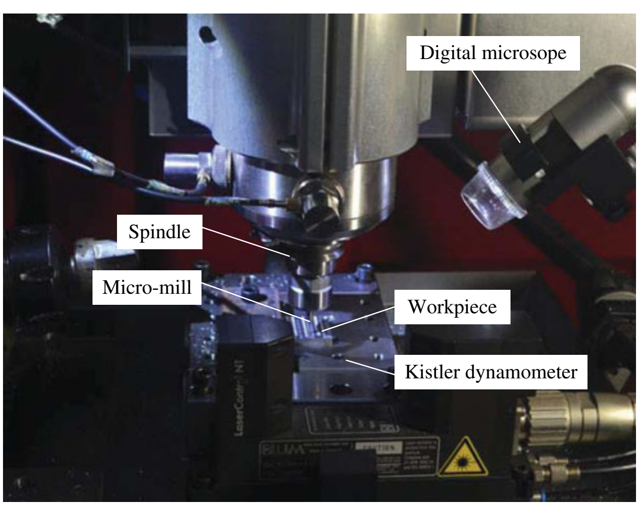


**Fig. 3** Experimental setup for micromilling tests

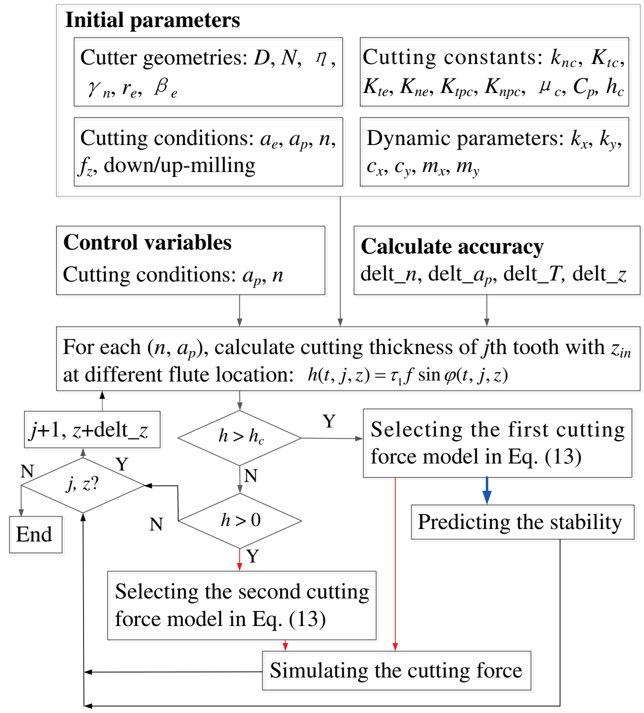


**Fig. 4** The flow chart for simulating cutting forces and predicting the stability

"red color" (i.e., cases (i), (j), (n), and (o)) are unstable; and other cases are stable (labeled in "blue and green colors"). According to the reference [32], for the stable cases, the cases (a) and (f) with spindle speed 10,000 rpm, and the cases (c), (h), and (m) with spindle speed 20,000 rpm, are located at the resonance region ($x$ direction: 10,139~10,261 rpm, and 20,278~20,523 rpm; $y$ direction: 9,254~9,347 rpm and 18,507~18,693 rpm), which are labeled in "green color".

Specify the spindle speed $n$ and axial depth of cut $a_p$ (listed in Table 4); the cutting forces and vibrating displacements can be obtained by using the above the simulating procedure, as shown in Figs. 6 and 7. Blue lines present the cutting forces and vibration displacements in $y$ direction, and green lines present those in $x$ direction, respectively. Similar to the results

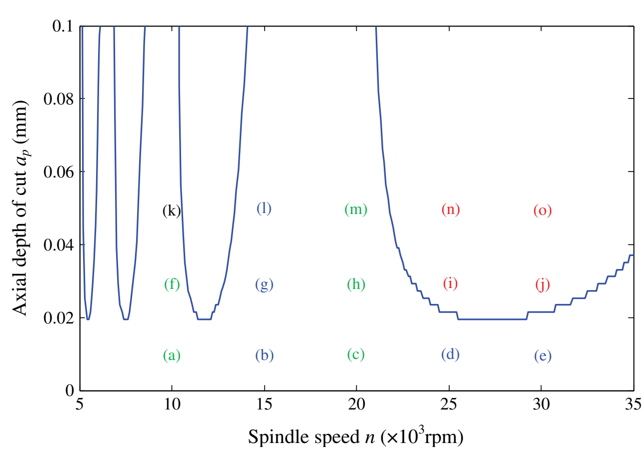


**Fig. 5** Stability diagram for micromilling process

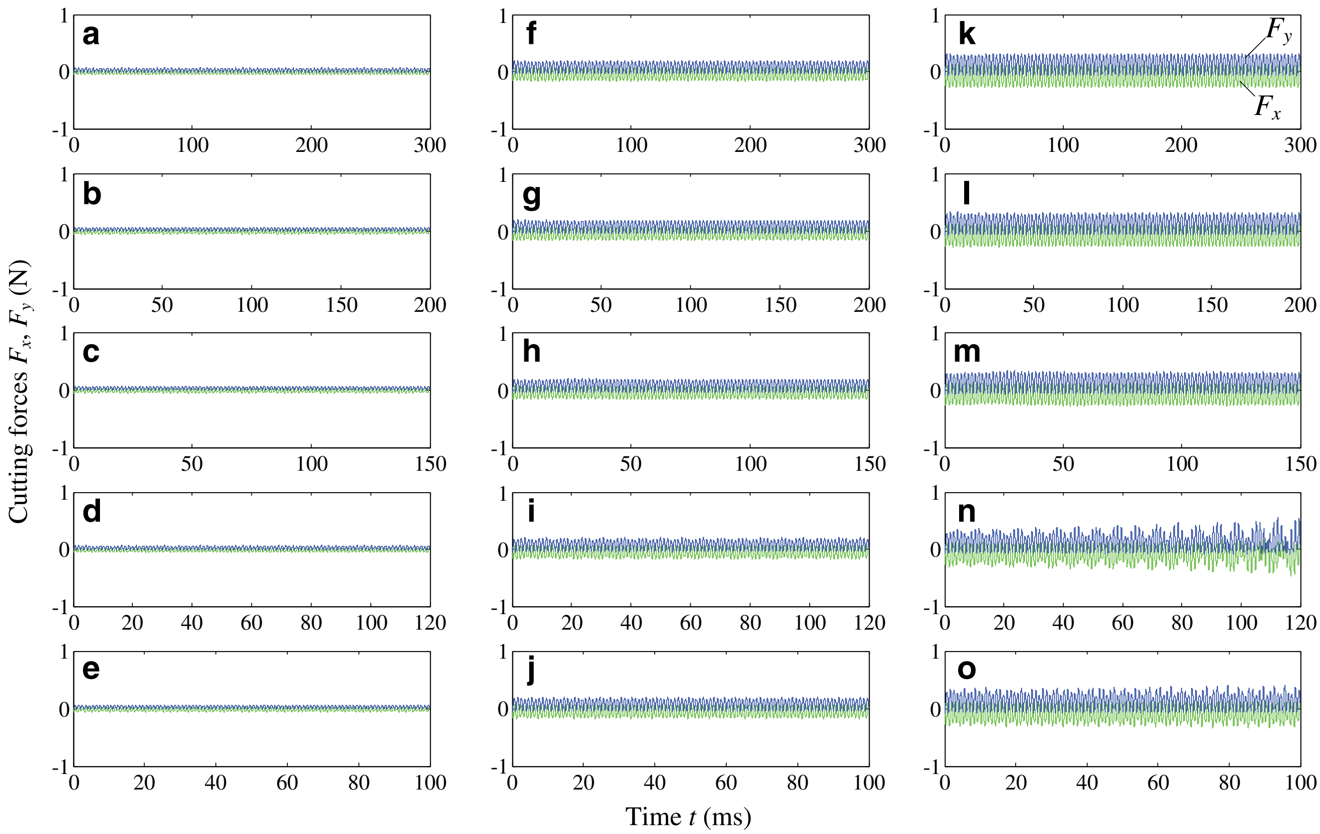


**Fig. 6** Cutting forces obtained by numerical method for 15 cutting cases

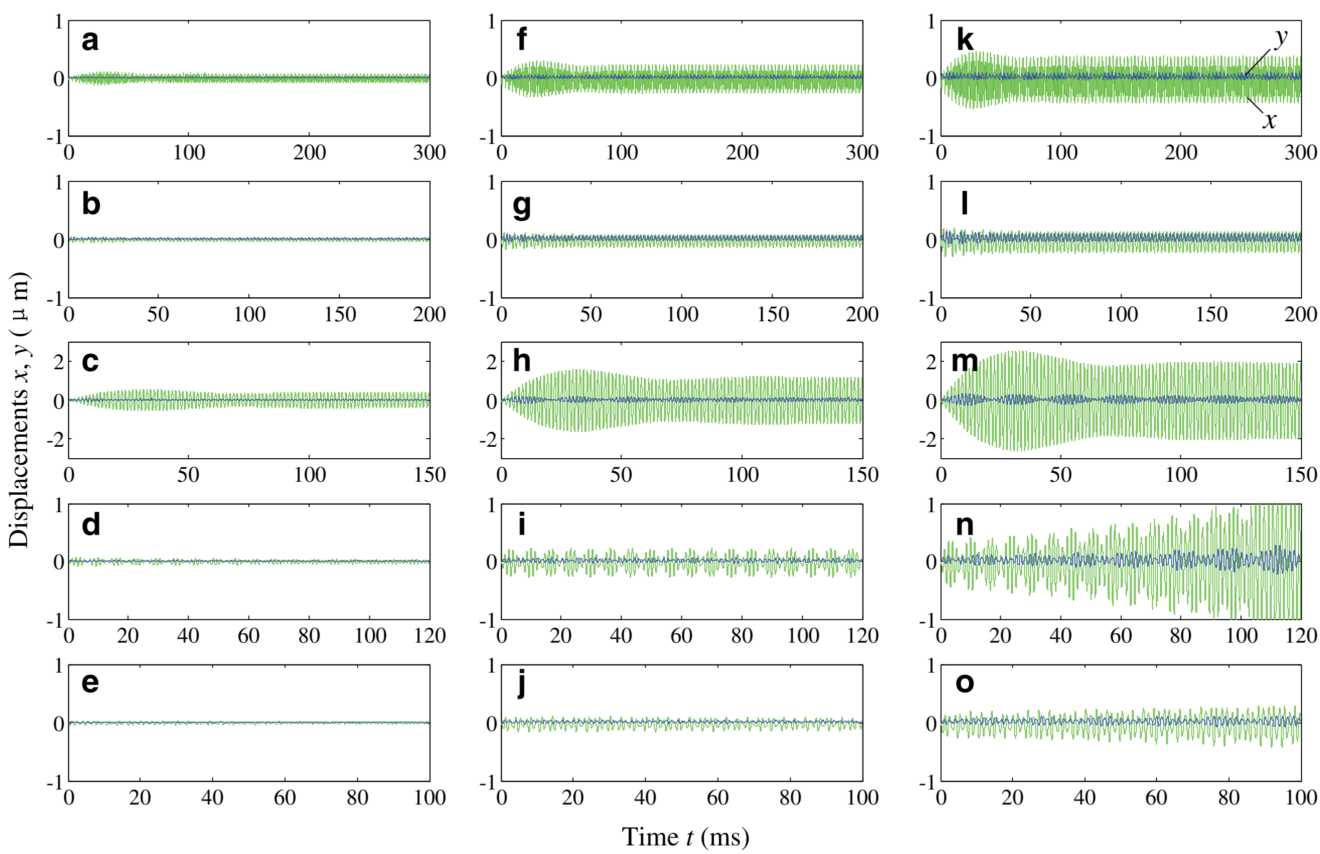


**Fig. 7** Vibration displacements obtained by numerical method for 15 cutting cases

which are obtained from Fig. 5, cases (i), (j), (n), and (o) are unstable, especially the cases (n) and (o) exhibit the intensively unstable characteristics; and other cases are stable. In Fig. 7, the results of cases (a), (f), (k), and (c), (h), (m) show the resonance occur in these conditions; while the processes for these cases are all still stable, because the displacements for these cases are all convergent with time, but not emanating. These characteristics for these cases are verified by the results of cutting forces and displacements shown in Figs. 6 and 7.

To valid the stability results, chatter tests were conducted under selected 15 cutting cases described in Section 3 and listed in Table 4. The experimental cutting forces results for 15 cutting conditions are rearranged and shown in Fig. 8 in order to comparing with each other. Similar as in Figs. 6 and 7, Blue lines present the cutting forces in $y$ direction, and green lines present those in $x$ direction, respectively. From Fig. 8, it is obvious that the cutting conditions (cases (i), (j), (n), and (o)) are unstable, other cases are stable except for the cases (k), (l), (h), (m).

From Figs. 5, 6, 7, and 8, in spite of some small quantitative discrepancies, experimental and theoretical results agree well except for the cases (k), (l), (h), (m). There might be several possible reasons for the small differences: (1) Uncertainty, there are uncertainty problems about the dynamic characteristics of system, cutting constants, materials of workpiece and tool, and so on, e.g., the values of the cutting force coefficients may also vary for different spindle speeds (the values used here were determined at constant spindle speed 16,000 rpm). Experiments have also showed that the dominant frequency of the tool system decreases as spindle speed is increased [33]. (2) Resonance vibration, in Fig. 7f, k, h, m exhibit the intensively resonance occurring. Studies about the relationship between resonance region and chatter region can be found in reference [32], in detail. (3) The critical chip thickness may also vary for different both cutting parameters and process parameters (the value used here was constant with 1 μm). Additionally, cutting thickness is calculated by using the approximation of $h=\tau_1 f\sin\varphi$, excluding regenerative displacements, in step 2 of simulating procedure (in Fig. 4). However, in spite of the approximations in the model, it should be emphasized that the experimental and theoretical results agree well in the presented parameter domains.

Machined workpiece surface are scanned through Digital Microscope (Keyence VHX-600ESO). The pictures for the surfaces in 15 cutting conditions listed in Table 4 are presented in Fig. 9 with lens ×200. For differential axial depths of cut, the burrs appeared in lower axial depth of cut are serious, e.g., (a)~(j) for $a_p$=0.01 and 0.03 mm; in higher axial depth of cut, while, burrs almost disappears, e.g., (k)~(o) for $a_p$=0.05 mm. With the same axial depth of cut, e.g., cases (a)~(e), and cases

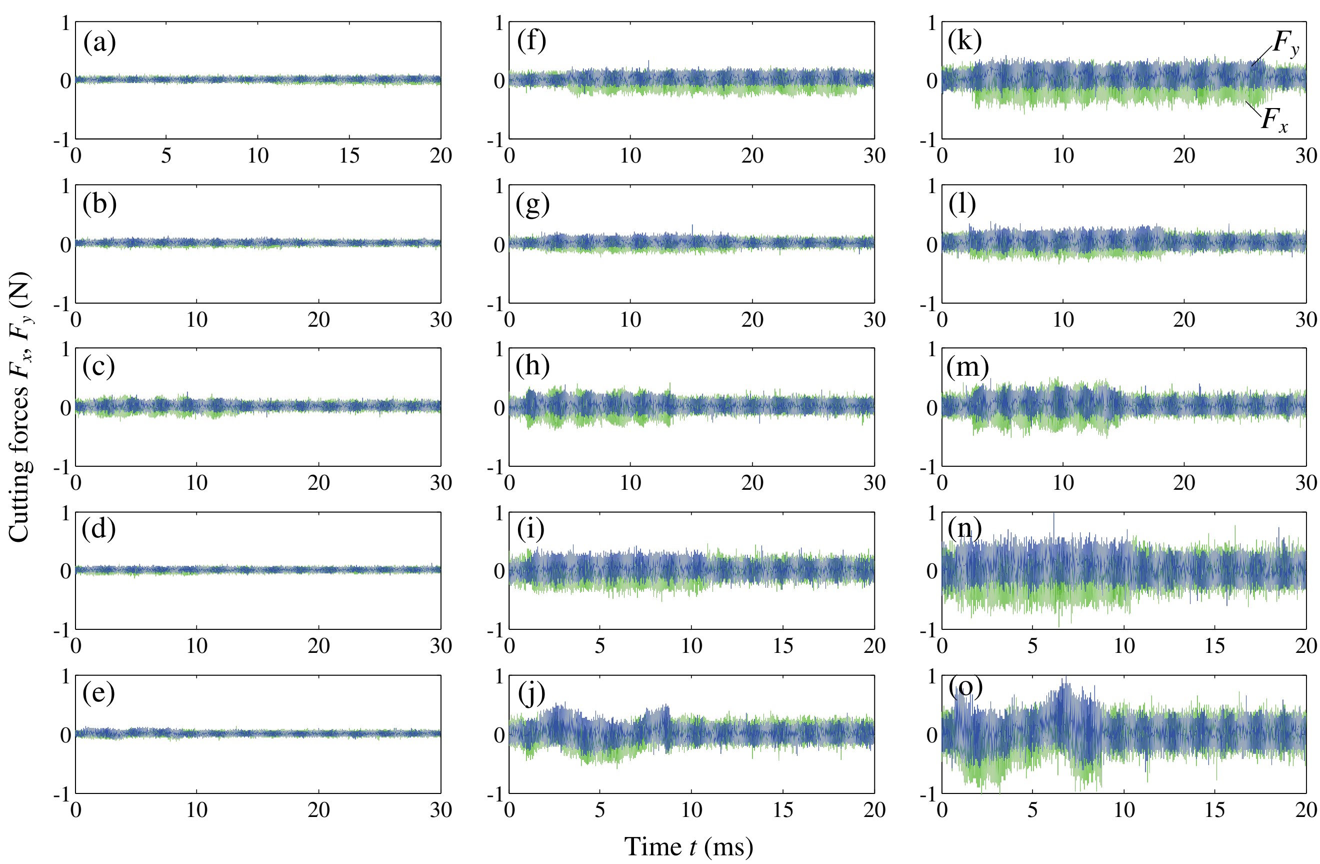


**Fig. 8** Experimental cutting forces for 15 cutting cases

(f)~(i), although it is not very obvious, the burrs occurred in speed $n$=20,000 rpm, are the more serious than those in other speeds, except for cases (f), (d), and (e). The process forming the burr is a complex phenomenon, and is associated with many factors, e.g., cutting parameters, workpiece properties, cutter parameters, and so on, especially, is dependent with the aerodynamic field around the cutter rotating with high speed [34]. The detailed analysis can be found in Ref. [35] or other literature. The content about burr is not concentration of this paper. While, it is noted that chatter or unstable cutting plays an important influence on the forming of burr. And on this viewpoint, for micromilling operations, there are two important contents that should be focused on in the future, one is that analyzing the relationship between the burr generation

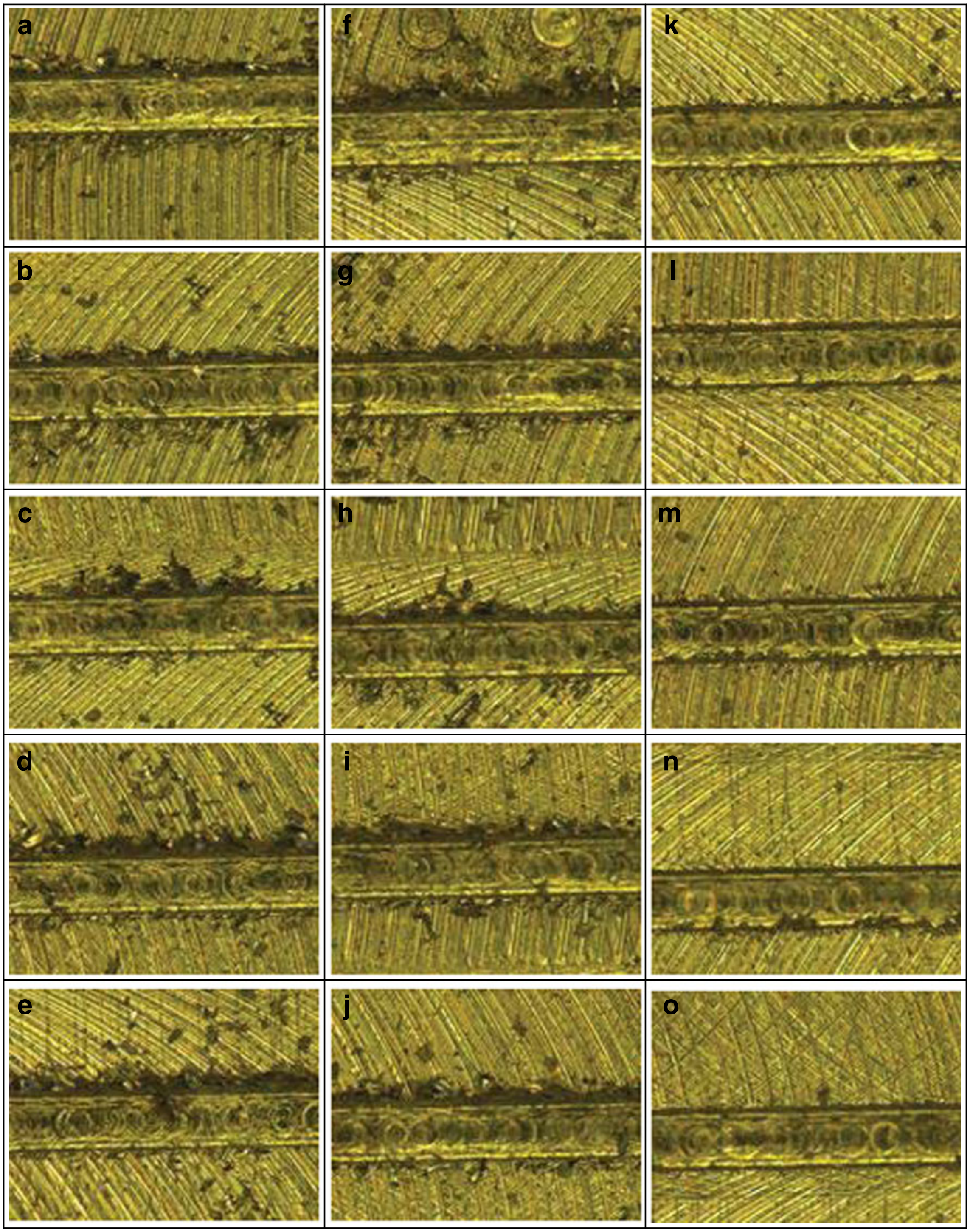


**Fig. 9** Pictures of the machined workpiece surface

mechanism and cutting vibration in future, the other is that conducting the investigation about aerodynamic field around the cutter rotating with high speed for burr forming and design of cutter, because the micromilling generally is operated in higher spindle speed.

## 5 Conclusions

A mechanistic model is developed to predict micromilling forces for both shearing and ploughing-dominant cutting regimes. The model assumes that there is a critical chip thickness that determines whether a chip will form or not. On the one hand, when machining is performed at high feed rates, the effects of ploughing and elastic recovery are insignificant enough to ignore, and the cutting mechanism is considered to be shearing. Numerical method is expanded to predict the chatter stability in micro end milling, which is conducted based on the proposed cutting force model. The simulating procedure for predicting stability and cutting forces is presented, and the stability diagram is constructed. The validation experiments are conducted to verify the simulation results. The experimental cutting forces measured are analyzed, and the machined workpiece surface scanned through digital microscope are also analyzed, especial the burr forming process. Further studies in micromilling operations are needed to investigate the relationship between the burr generation mechanism and cutting vibration, and the aerodynamic field around the cutter rotating with high speed for burr forming and design of cutter.

**Acknowledgments** The authors are grateful to the financial supports of the National Natural Science Foundation of China (no. 51205233) and the Research Award fund for Outstanding Young Scientists of Shandong Province (no. BS2013ZZ013).

## Appendix

1. If $h>h_c$, transforming the cutting forces (the first equation in Eq. (12)) from the cutter coordinates to the global coordinates, obtained

$$
\begin{Bmatrix} \Delta F_x^j(z,t) \\ \Delta F_y^j(z,t) \\ \Delta F_z^j(z,t) \end{Bmatrix} = \begin{bmatrix} -\sin\varphi(t,j,z) & -\cos\varphi(t,j,z) & 0 \\ -\cos\varphi(t,j,z) & \sin\varphi(t,j,z) & 0 \\ 0 & 0 & 1 \end{bmatrix} \begin{Bmatrix} \Delta F_\mathrm{r}^j(t) \\ \Delta F_\mathrm{t}^j(t) \\ \Delta F_\mathrm{z}^j(t) \end{Bmatrix}
$$

$$
= \left( \begin{bmatrix} \mathrm{DK}_{11}^j(z,t) & \mathrm{DK}_{12}^j(z,t) \\ \mathrm{DK}_{21}^j(z,t) & \mathrm{DK}_{22}^j(z,t) \\ \mathrm{DK}_{31}^j(z,t) & \mathrm{DK}_{32}^j(z,t) \end{bmatrix} \begin{Bmatrix} A(t) \\ B(t) \end{Bmatrix} + \begin{bmatrix} \mathrm{DC}_{11}^j(z,t) & \mathrm{DC}_{12}^j(z,t) \\ \mathrm{DC}_{21}^j(z,t) & \mathrm{DC}_{22}^j(z,t) \\ \mathrm{DC}_{31}^j(z,t) & \mathrm{DC}_{32}^j(z,t) \end{bmatrix} \begin{Bmatrix} \dot{A}(t) \\ \dot{B}(t) \end{Bmatrix} + \begin{Bmatrix} \mathrm{DE}_1^j(z,t) \\ \mathrm{DE}_2^j(z,t) \\ \mathrm{DE}_3^j(z,t) \end{Bmatrix} \right) \Delta z \tag{A.1}
$$

where

$$
\begin{Bmatrix} \mathrm{DK}_{11}^j(z,t) \\ \mathrm{DK}_{12}^j(z,t) \\ \mathrm{DK}_{21}^j(z,t) \\ \mathrm{DK}_{22}^j(z,t) \\ \mathrm{DK}_{31}^j(z,t) \\ \mathrm{DK}_{32}^j(z,t) \end{Bmatrix} = \begin{bmatrix} -k_1K_\mathrm{tc} & -\left(k_2K_\mathrm{tc}+k_1C_\mathrm{p}\Omega\right) & -k_2C_\mathrm{p}\Omega & 0 & 0 \\ k_1C_\mathrm{p}\Omega & \left(k_2C_\mathrm{p}\Omega - k_1K_\mathrm{tc}\right) & -k_2K_\mathrm{tc} & 0 & 0 \\ k_2K_\mathrm{tc} & \left(k_2C_\mathrm{p}\Omega - k_1K_\mathrm{tc}\right) & -k_1C_\mathrm{p}\Omega & 0 & 0 \\ -k_2C_\mathrm{p}\Omega & \left(k_2K_\mathrm{tc}+k_1C_\mathrm{p}\Omega\right) & -k_1K_\mathrm{tc} & 0 & 0 \\ 0 & 0 & 0 & k_3K_\mathrm{tc} & k_3C_\mathrm{p}\Omega \\ 0 & 0 & 0 & -k_3C_\mathrm{p}\Omega & k_3K_\mathrm{tc} \end{bmatrix} \begin{Bmatrix} \sin^2\varphi(t,j,z) \\ \frac{1}{2}\sin2\varphi(t,j,z) \\ \cos^2\varphi(t,j,z) \\ \sin\varphi(t,j,z) \\ \cos\varphi(t,j,z) \end{Bmatrix} \tag{A.2}
$$

$$
= \Lambda \begin{Bmatrix} \sin^2\varphi(t,j,z) \\ \frac{1}{2}\sin2\varphi(t,j,z) \\ \cos^2\varphi(t,j,z) \\ \sin\varphi(t,j,z) \\ \cos\varphi(t,j,z) \end{Bmatrix}
$$

$$\begin{Bmatrix} \mathrm{DC}_{11}^{j}(z,t) \\ \mathrm{DC}_{12}^{j}(z,t) \\ \mathrm{DC}_{21}^{j}(z,t) \\ \mathrm{DC}_{22}^{j}(z,t) \\ \mathrm{DC}_{31}^{j}(z,t) \\ \mathrm{DC}_{32}^{j}(z,t) \end{Bmatrix} = \begin{bmatrix} -k_1C_\mathrm{p} & -k_2C_\mathrm{p} & 0 & 0 & 0 \\ 0 & -k_1C_\mathrm{p} & -k_2C_\mathrm{p} & 0 & 0 \\ k_2C_\mathrm{p} & -k_1C_\mathrm{p} & 0 & 0 & 0 \\ 0 & k_2C_\mathrm{p} & -k_1C_\mathrm{p} & 0 & 0 \\ 0 & 0 & 0 & k_3C_\mathrm{p} & 0 \\ 0 & 0 & 0 & 0 & k_3C_\mathrm{p} \end{bmatrix} \begin{Bmatrix} \sin^2\varphi(t,j,z) \\ \frac{1}{2}\sin 2\varphi(t,j,z) \\ \cos^2\varphi(t,j,z) \\ \sin\varphi(t,j,z) \\ \cos\varphi(t,j,z) \end{Bmatrix} = \Gamma \begin{Bmatrix} \sin^2\varphi(t,j,z) \\ \frac{1}{2}\sin 2\varphi(t,j,z) \\ \cos^2\varphi(t,j,z) \\ \sin\varphi(t,j,z) \\ \cos\varphi(t,j,z) \end{Bmatrix} \tag{A.3}$$

$$\begin{Bmatrix} \mathrm{DE}_{1}^{j}(z,t) \\ \mathrm{DE}_{2}^{j}(z,t) \\ \mathrm{DE}_{3}^{j}(z,t) \end{Bmatrix} = \begin{bmatrix} -K_\mathrm{re} & -K_\mathrm{te} & 0 \\ K_\mathrm{te} & -K_\mathrm{re} & 0 \\ 0 & 0 & K_\mathrm{ze} \end{bmatrix} \begin{Bmatrix} \sin\varphi(t,j,z) \\ \cos\varphi(t,j,z) \\ 1 \end{Bmatrix} = \Theta \begin{Bmatrix} \sin\varphi(t,j,z) \\ \cos\varphi(t,j,z) \\ 1 \end{Bmatrix} \tag{A.4}$$

Integrating Eq. (A.1) with respect to $z$, obtained

$$\begin{Bmatrix} F_x^j(t) \\ F_y^j(t) \\ F_z^j(t) \end{Bmatrix} = \int_{z_1}^{z_2} \begin{Bmatrix} \mathrm{d}F_x^j(z,t) \\ \mathrm{d}F_y^j(z,t) \\ \mathrm{d}F_z^j(z,t) \end{Bmatrix} = \begin{bmatrix} K_{11}^j(t) & K_{12}^j(t) \\ K_{21}^j(t) & K_{22}^j(t) \\ K_{31}^j(t) & K_{32}^j(t) \end{bmatrix} \begin{Bmatrix} A(t) \\ B(t) \end{Bmatrix} + \begin{bmatrix} C_{11}^j(t) & C_{12}^j(t) \\ C_{21}^j(t) & C_{22}^j(t) \\ C_{31}^j(t) & C_{32}^j(t) \end{bmatrix} \begin{Bmatrix} \dot{A}(t) \\ \dot{B}(t) \end{Bmatrix} + \begin{Bmatrix} E_1^j(t) \\ E_2^j(t) \\ E_3^j(t) \end{Bmatrix} \tag{A.5}$$

where

$$\begin{bmatrix} K_{11}^j(t) & K_{12}^j(t) \\ K_{21}^j(t) & K_{22}^j(t) \\ K_{31}^j(t) & K_{32}^j(t) \end{bmatrix} = \Lambda \begin{Bmatrix} \mathrm{ss}(t,j) \\ \mathrm{sc}(t,j) \\ \mathrm{cc}(t,j) \\ s(t,j) \\ c(t,j) \end{Bmatrix}, \begin{bmatrix} C_{11}^j(t) & C_{12}^j(t) \\ C_{21}^j(t) & C_{22}^j(t) \\ C_{31}^j(t) & C_{32}^j(t) \end{bmatrix} = \Gamma \begin{Bmatrix} \mathrm{ss}(t,j) \\ \mathrm{sc}(t,j) \\ \mathrm{cc}(t,j) \\ s(t,j) \\ c(t,j) \end{Bmatrix}, \begin{Bmatrix} E_1^j(t) \\ E_2^j(t) \\ E_3^j(t) \end{Bmatrix} = \Theta \begin{Bmatrix} s(t,j) \\ c(t,j) \\ \Delta z \end{Bmatrix} \tag{A.6}$$

here

$$\begin{gathered} \mathrm{ss}(t,j) = \int_{z_1}^{z_2} \sin^2\varphi(t,j,z)\mathrm{d}z, sc(t,j) = \int_{z_1}^{z_2} \frac{1}{2}\sin 2\varphi(t,j,z)\mathrm{d}z, cc(t,j) = \int_{z_1}^{z_2} \cos^2\varphi(t,j,z)\mathrm{d}z, \\ s(t,j) = \int_{z_1}^{z_2} \sin\varphi(t,j,z)\mathrm{d}z, c(t,j) = \int_{z_1}^{z_2} \cos\varphi(t,j,z)\mathrm{d}z \end{gathered} \tag{A.7}$$

Summing the cutting forces over all of the $N$ number of teeth,

$$\begin{Bmatrix} F_x(t) \\ F_y(t) \\ F_z(t) \end{Bmatrix} = \sum_{j=1}^{N} \begin{Bmatrix} F_x^j(t) \\ F_y^j(t) \\ F_z^j(t) \end{Bmatrix} = \sum_{j=1}^{N} \begin{bmatrix} K_{11}^j(t) & K_{12}^j(t) \\ K_{21}^j(t) & K_{22}^j(t) \\ K_{31}^j(t) & K_{32}^j(t) \end{bmatrix} \begin{Bmatrix} A(t) \\ B(t) \end{Bmatrix} + \sum_{j=1}^{N} \begin{bmatrix} C_{11}^j(t) & C_{12}^j(t) \\ C_{21}^j(t) & C_{22}^j(t) \\ C_{31}^j(t) & C_{32}^j(t) \end{bmatrix} \begin{Bmatrix} \dot{A}(t) \\ \dot{B}(t) \end{Bmatrix} + \sum_{j=1}^{N} \begin{Bmatrix} E_1^j(t) \\ E_2^j(t) \\ E_3^j(t) \end{Bmatrix}$$

$$= \begin{bmatrix} K_{11}(t) & K_{12}(t) \\ K_{21}(t) & K_{22}(t) \\ K_{31}(t) & K_{32}(t) \end{bmatrix} \begin{Bmatrix} A(t) \\ B(t) \end{Bmatrix} + \begin{bmatrix} C_{11}(t) & C_{12}(t) \\ C_{21}(t) & C_{22}(t) \\ C_{31}(t) & C_{32}(t) \end{bmatrix} \begin{Bmatrix} \dot{A}(t) \\ \dot{B}(t) \end{Bmatrix} + \begin{Bmatrix} E_1(t) \\ E_2(t) \\ E_3(t) \end{Bmatrix}$$

$$= \begin{bmatrix} K_{11}(t) & K_{12}(t) \\ K_{21}(t) & K_{22}(t) \\ K_{31}(t) & K_{32}(t) \end{bmatrix} \begin{Bmatrix} q_x(t) - q_x(t-\tau_1) + q_u(t) - q_u(t-\tau_1) + \tau_1 f \\ q_y(t) - q_y(t-\tau_2) + q_v(t) - q_v(t-\tau_2) \end{Bmatrix}$$

$$+ \begin{bmatrix} C_{11}(t) & C_{12}(t) \\ C_{21}(t) & C_{22}(t) \\ C_{31}(t) & C_{32}(t) \end{bmatrix} \begin{Bmatrix} \dot{q}_x(t) - \dot{q}_x(t-\tau_1) + \dot{q}_u(t) - \dot{q}_u(t-\tau_1) \\ \dot{q}_y(t) - \dot{q}_y(t-\tau_2) + \dot{q}_v(t) - \dot{q}_v(t-\tau_2) \end{Bmatrix} + \begin{Bmatrix} E_1(t) \\ E_2(t) \\ E_3(t) \end{Bmatrix}$$

$$= \begin{bmatrix} K_{11}(t) & K_{12}(t) & K_{11}(t) & K_{12}(t) \\ K_{21}(t) & K_{22}(t) & K_{21}(t) & K_{22}(t) \\ K_{11}(t) & K_{12}(t) & K_{11}(t) & K_{12}(t) \\ K_{21}(t) & K_{22}(t) & K_{21}(t) & K_{22}(t) \end{bmatrix} \begin{Bmatrix} q_x(t) \\ q_y(t) \\ q_u(t) \\ q_v(t) \end{Bmatrix} - \begin{bmatrix} K_{11}(t) & K_{12}(t) & K_{11}(t) & K_{12}(t) \\ K_{21}(t) & K_{22}(t) & K_{21}(t) & K_{22}(t) \\ K_{11}(t) & K_{12}(t) & K_{11}(t) & K_{12}(t) \\ K_{21}(t) & K_{22}(t) & K_{21}(t) & K_{22}(t) \end{bmatrix} \begin{Bmatrix} q_x(t-\tau_1) \\ q_y(t-\tau_2) \\ q_u(t-\tau_1) \\ q_v(t-\tau_2) \end{Bmatrix} + \begin{Bmatrix} K_{11}(t) \\ K_{21}(t) \\ K_{11}(t) \\ K_{21}(t) \end{Bmatrix} \tau_1 f$$

$$+ \begin{bmatrix} C_{11}(t) & C_{12}(t) & C_{11}(t) & C_{12}(t) \\ C_{21}(t) & C_{22}(t) & C_{21}(t) & C_{22}(t) \\ C_{11}(t) & C_{12}(t) & C_{11}(t) & C_{12}(t) \\ C_{21}(t) & C_{22}(t) & C_{21}(t) & C_{22}(t) \end{bmatrix} \begin{Bmatrix} q_x(t) \\ q_y(t) \\ q_u(t) \\ q_v(t) \end{Bmatrix} - \begin{bmatrix} C_{11}(t) & C_{12}(t) & C_{11}(t) & C_{12}(t) \\ C_{21}(t) & C_{22}(t) & C_{21}(t) & C_{22}(t) \\ C_{11}(t) & C_{12}(t) & C_{11}(t) & C_{12}(t) \\ C_{21}(t) & C_{22}(t) & C_{21}(t) & C_{22}(t) \end{bmatrix} \begin{Bmatrix} q_x(t-\tau_1) \\ q_y(t-\tau_2) \\ q_u(t-\tau_1) \\ q_v(t-\tau_2) \end{Bmatrix} + \begin{Bmatrix} E_1(t) \\ E_2(t) \\ E_3(t) \end{Bmatrix}$$

$$= \mathbf{K}(t)\mathbf{q}(t) - \mathbf{K}(t)\mathbf{q}(t-\tau_{1,2}) + \widehat{\mathbf{K}}(t)\tau_1 f + \mathbf{C}(t)\dot{\mathbf{q}}(t) - \mathbf{C}(t)\dot{\mathbf{q}}(t-\tau_{1,2}) + \mathbf{E}(t) \tag{A.8}$$

2. If $0 < h \leq h_c$, transforming the cutting forces (the first equation in Eq. (12)) from the cutter coordinates to the global coordinates, obtained

$$\begin{Bmatrix} \Delta F_x^j(z,t) \\ \Delta F_y^j(z,t) \\ \Delta F_z^j(z,t) \end{Bmatrix} = \begin{bmatrix} -\sin\varphi(t,j,z) & -\cos\varphi(t,j,z) & 0 \\ -\cos\varphi(t,j,z) & \sin\varphi(t,j,z) & 0 \\ 0 & 0 & 1 \end{bmatrix} \left( \begin{Bmatrix} K_{\mathrm{rpc}} \\ K_{\mathrm{tpc}} \\ K_{\mathrm{apc}} \end{Bmatrix} A_{\mathrm{p}} + \begin{Bmatrix} K_{\mathrm{re}} \\ K_{\mathrm{te}} \\ K_{\mathrm{ae}} \end{Bmatrix} \right) \Delta z$$

$$= \left( \begin{Bmatrix} \mathrm{DP}_1^j(z,t) \\ \mathrm{DP}_2^j(z,t) \\ \mathrm{DP}_3^j(z,t) \end{Bmatrix} A_{\mathrm{p}} + \begin{Bmatrix} \mathrm{DE}_1^j(z,t) \\ \mathrm{DE}_2^j(z,t) \\ \mathrm{DE}_3^j(z,t) \end{Bmatrix} \right) \Delta z \tag{A.9}$$

where

$$\begin{Bmatrix} \mathrm{DP}_1^j(z,t) \\ \mathrm{DP}_2^j(z,t) \\ \mathrm{DP}_3^j(z,t) \end{Bmatrix} = \begin{bmatrix} -K_{\mathrm{rpc}} & -K_{\mathrm{tpc}} & 0 \\ K_{\mathrm{tpc}} & -K_{\mathrm{rpc}} & 0 \\ 0 & 0 & K_{\mathrm{apc}} \end{bmatrix} \begin{Bmatrix} \sin\varphi(t,j,z) \\ \cos\varphi(t,j,z) \\ 1 \end{Bmatrix} \tag{A.10}$$

Integrating Eq. (A.8) with respect to $z$, obtained

$$\begin{Bmatrix} F_x^j(t) \\ F_y^j(t) \\ F_z^j(t) \end{Bmatrix} = \int_{z_1}^{z_2} \begin{Bmatrix} \mathrm{d}F_x^j(z,t) \\ \mathrm{d}F_y^j(z,t) \\ \mathrm{d}F_z^j(z,t) \end{Bmatrix} = \begin{Bmatrix} P_1^j(t) \\ P_2^j(t) \\ P_3^j(t) \end{Bmatrix} A_{\mathrm{p}} + \begin{Bmatrix} E_1^j(t) \\ E_2^j(t) \\ E_3^j(t) \end{Bmatrix} \tag{A.11}$$

where

$$\begin{Bmatrix} P_1^j(t) \\ P_2^j(t) \\ P_3^j(t) \end{Bmatrix} = \Upsilon \begin{Bmatrix} s(t,j) \\ c(t,j) \\ \Delta z \end{Bmatrix} \tag{A.12}$$

Summing the cutting forces over all of the $N$ number of teeth,

$$\begin{aligned} \begin{Bmatrix} F_x(t) \\ F_y(t) \\ F_z(t) \end{Bmatrix} &= \sum_{j=1}^{N} \begin{Bmatrix} F_x^j(t) \\ F_y^j(t) \\ F_z^j(t) \end{Bmatrix} \\ &= \sum_{j=1}^{N} \begin{Bmatrix} P_1^j(t) \\ P_2^j(t) \\ P_3^j(t) \end{Bmatrix} A_{\mathrm{p}} + \sum_{j=1}^{N} \begin{Bmatrix} E_1^j(t) \\ E_2^j(t) \\ E_3^j(t) \end{Bmatrix} \\ &= \begin{Bmatrix} P_1(t) \\ P_2(t) \\ P_3(t) \end{Bmatrix} A_{\mathrm{p}} + \begin{Bmatrix} E_1(t) \\ E_2(t) \\ E_3(t) \end{Bmatrix} = \mathbf{P}(t) A_{\mathrm{p}} + \mathbf{E}(t) \end{aligned} \tag{A.13}$$

## References


1. Chae J, Park SS, Freiheit T (2006) Investigation of micro-cutting operations. Int J Mach Tools Manuf 46(3–4):313–332
2. Dornfeld D, Min S, Takeuchi T (2006) Recent advances in mechanical micro-machining. CIRP Ann Manuf Technol 55(2):745–768
3. Kang IS, Kim JS, Kim JH, Kang MC, Seo YW (2007) A mechanistic model of cutting force in the micro end milling process. J Mater Proc Technol 187–188:250–255
4. Miao JC, Chen GL, Lai XM, Li HT, Li CF (2007) Review of dynamic issues in micro-end-milling. Int J Adv Manuf Technol 31: 897–904
5. Mascardelli B, Park SS, Freiheit T (2008) Substructure coupling of micro end mills to aid in the suppression of chatter. ASME J Manuf Sci Eng 130(1):011010
6. Vogler MP, DeVor RE, Kapoor SG (2003) Microstructure-level force prediction model for micro-milling of multi-phase materials. ASME J Manuf Sci Eng 125(2):202–209
7. Jawahir IS, Ee KC, Dillon OW Jr (2005) Finite element modeling of residual stresses in machining induced by cutting using a tool with finite edge radius. Int J Mech Sci 47(10):1611–1628
8. Lai X, Li H, Li C, Lin Z, Ni J (2008) Modelling and analysis of micro scale milling considering size effect, micro cutter edge radius and minimum chip thickness. Int J Mach Tools Manuf 48:1–14
9. Bissacco G, Hansen HN, Slunsky J (2008) Modelling the cutting edge radius size effect for force prediction in micro milling. CIRP Ann Manuf Technol 57(1):113–116
10. Shi ZY, Liu ZQ (2010) The actual geometry of the cutting tool involved in machining. Int J Adv Manuf Technol 46:91–99
11. Liu K, Melkote SN (2006) Material strengthening mechanisms and their contribution to size effect in micro-cutting. ASME J Manuf Sci Eng 128(3):730–738
12. Vogler MP, Kapoor SG, DeVor RE (2004) On the modeling and analysis of machining performance in micro end milling, part II: cutting force prediction. ASME J Manuf Sci Eng 126(4):695–705
13. Jun MBG, Liu X, DeVor RE, Kapoor SG (2006) Investigation of the dynamics of micro end milling, part 1: model development. ASME J Manuf Sci Eng 128(4):893–900
14. Fang N (2003) Slip-line modeling of machining with a rounded-edge tool-part I: new model and theory. J Mech Phys Solids 51(4):715–742
15. Zaman MT, Kumar AS, Rahman M, Sreeram S (2006) A three-dimensional analytical cutting force model for micro end milling operation. Int J Mach Tools Manuf 46(3–4):353–366
16. Bao WY, Tansel IN (2000) Modeling micro end-milling operations, part I: analytical cutting force model. Int J Mach Tools Manuf 40(15): 2155–2173
17. Lee HU, Cho DE, Ehmann KF (2008) A mechanistic model of cutting forces in micro-end-milling with cutting-condition-independent cutting force coefficients. ASME J Manuf Sci Eng 130(3):0311021–0311029
18. Lakshmi LS, Vasu V, Krishna P, Rao BN, Rakesh S (2008) Analytical prediction of stability lobes in high-speed milling and their application to micromilling. Int J Manuf Technol Manag 13(2–4):146–168
19. Shi Y, Frederik M, von Utz W, Eckart U (2013) Gyroscopic and mode interaction effects on micro-end mill dynamics and chatter stability. Int J Adv Manuf Technol 65(5–8):895–907
20. Afazov SM, Ratchev SM, Segal J, Popov AA (2012) Chatter modelling in micro-milling by considering process nonlinearities. Int J Mach Tools Manuf 56:28–38
21. Malekian M, Park SS, Jun MBG (2009) Modeling of dynamic micro-milling cutting forces. Int J Mach Tools Manuf 49(7–8): 586–598
22. Shi Y, Frederik M, von Utz W, Eckart U (2012) Chatter frequencies of micromilling processes: influencing factors and online detection via piezoactuators. Int J Mach Tools Manuf 56:10–16
23. Tajalli SA, Movahhedy MR, Akbari J (2012) Investigation of the effects of process damping on chatter instability in micro end milling. Procedia CIRP 1:156–161
24. Rahnama R, Sajjadi M, Park SS (2009) Chatter suppression in micro end milling with process damping. J Mater Proc Technol 209:5766–5776
25. Park SS, Rahnama R (2010) Robust chatter stability in micro-milling operations. CIRP Annals Manuf Technol 59:391–394
26. Faassen RPH, van de Wouw N, Nijmeijer H, Oosterling JAJ (2007) An improved tool path model including periodic delay for chatter prediction in milling. J Comput Nonlinear Dyn 2(2):167–179

27. Balachandran B, Zhao X (2000) A mechanics based model for study for study of dynamics of milling operations. Meccanica 35:89–109
28. Altintas Y, Lee P (1996) A general mechanics and dynamics model for helical end mills. CIRP Ann Manuf Technol 45(1):59–64
29. Malekian M, Park SS (2007) Investigation of micro milling forces for aluminum. Trans SME NAMRI 35(1):417–424
30. Insperger T, Stepan G (2002) Semi-discretization method for delayed systems. Int J Numer Methods Eng 55:503–518
31. Bayly PV, Halley JE, Mann BP, Davies MA (2003) Stability of interrupted cutting by temporal finite element analysis. ASME J Manuf Sci Eng 125:220–225
32. Song QH, Ai X, Zhao J (2011) Design for variable pitch end mills with high milling stability. Int J Adv Manuf Technol 55: 891–903
33. Gradišek J, Kalveram M, Insperger T, Weinert K, Stépán G, Govekar E, Grabec I (2005) On stability prediction for milling. Int J Mach Tools Manuf 45(7–8):741–991
34. Ji CH, Liu ZQ (2012) Numerical analysis of aeroacoustic noise for high-speed face milling cutters in three dimensional unsteady flow fields. ASME J Manuf Sci Eng 134:041002
35. Zhang T, Liu ZQ, Xu CH (2013) Influence of size effect on burr formation in micro cutting. Int J Adv Manuf Technol 68(9–12):1911–1917